On the S/W stoichiometry and triboperformance of WSxC(H) coatings deposited by magnetron sputtering

Cao, Huatang; Wen, Feng; Kumar, Sumit; Rudolf, Petra; De Hosson, Jeff Th. M.; Pei, Yutao

Published in:
Surface & Coatings Technology

DOI:
10.1016/j.surfcoat.2018.04.040

Surface & Coatings Technology 365 (2019) 41–51

Contents lists available at ScienceDirect

Surface & Coatings Technology

journal homepage: www.elsevier.com/locate/surfcoat

On the S/W stoichiometry and triboperformance of $WS_xC(H)$ coatings deposited by magnetron sputtering

Huatang Cao[a], Feng Wen[a], Sumit Kumar[b], Petra Rudolf[b], Jeff Th.M. De Hosson[c], Yutao Pei[a,*]

[a] Department of Advanced Production Engineering, Engineering and Technology Institute Groningen, University of Groningen, Nijenborgh 4, 9747AG, The Netherlands
[b] Department of Surfaces and Thin Films, Zernike Institute for Advanced Materials, University of Groningen, Nijenborgh 4, 9747AG Groningen, The Netherlands
[c] Department of Applied Physics, Zernike Institute for Advanced Materials, University of Groningen, Nijenborgh 4, 9747AG Groningen, The Netherlands

ARTICLE INFO

Keywords:
WS_2
Coating
Target-substrate distance
Magnetron cosputtering and reactive sputtering
Stoichiometry
Tribology

ABSTRACT

$WS_xC(H)$ coatings were deposited on single crystal silicon(100) wafers by magnetron co-sputtering and reactive sputtering at various target-substrate distances. Upon increasing the distance, the stoichiometric S/W ratio increases from 0.51 to 1.89. Also, the porosity of coatings gradually augments and a columnar microstructure tends to form. Preferential sulfur resputtering rather than contaminations primarily accounts for the low S/W ratio. TEM reveals randomly oriented WS_2(002) platelets in the WS_xC coatings when deposited at a large distance, which is supported by XRD. The composite coatings exhibit a decreasing hardness and elastic modulus with increasing target-substrate distance. The triboperformance is strongly affected by the coating composition, the target-substrate distance and the testing environment. Cross-sectional TEM of formed tribofilms reveals an obvious reorientation of WS_2(002) basal planes parallel to the plane of sliding, leading to an ultralow friction.

1. Introduction

WS_2 belongs to the class of layered transition metal dichalcogenides (TMD) and has drawn considerable attention owing to its excellent solid lubrication properties. WS_2 crystallizes in the hexagonal structure where a layer of tungsten atoms is sandwiched between two hexagonally packed sulfur layers. While the bonding within the layer is covalent, the bonding between the adjacent layer consists of weak Van der Waals interactions [1]. The electronic structure of this TMD results in a small positive net charge outside of the lamellae, leading to an electrostatic repulsion between the (002) hexagonal basal planes and thus offering an easy planar glide [2]. In fact, sliding can readily shear TMD crystals to generate clean and atomically smooth surfaces [3]. Even amorphous WS_2 can be crystallized and basal planes are realigned along the sliding direction, offering an ultralow coefficient of friction (CoF) [4,5]. Therefore, sputtered TMD coatings have been widely used in transport industry, particularly in high vacuum aerospace environment [6,7]. However, TMDs' lubricating properties usually degrade through oxidizing in moisture and are also limited by their low bearing capacity. Various third elements (e.g. Ti [8], Cr [9], Al [10], Pb [11], Ni [12], C [13]) were incorporated to reduce oxidation and improve the triboperformance. Among them, the nanocomposite MeY_2/a-C coatings (where Me is Mo or W, and Y is S or Se), namely MeY_2 lamellae embedded in an amorphous diamond-like carbon (DLC) matrix, have demonstrated excellent tribological characteristics, with both a low CoF and a high wear resistance over a wide range of humidities [14,15]. Voevodin *et al.* [15,16] even pioneered a "chameleon" WC/WS_2/DLC coating, where WS_2 aims at providing low friction in dry atmospheres, while the carbon matrix provides low friction in humid environments.

One negative aspect of magnetron sputtering high-quality MeY_2/a-C coating is that the MeY_x/a-C is usually sub-stoichiometric, with $x < 2$ [6,17] and this potentially impairs the tribological behaviors, for instance created by the sulfur deficiency in a MeS_2/a-C coating. Voevodin *et al.* [6] indicated that the WS_2/a-C composite with sulfur content < 15 at.% had a surprisingly high CoF of 0.5–0.7 in vacuum and 0.2–0.3 in dry nitrogen, consistent with the tribological behavior of single-phase unhydrogenated DLC in vacuum. A low Y/Me ratio is generally attributed to the preferential resputtering of Y due to the bombardment of energetic particles reflected on the coatings [18–21] and the reactions between MeY_2 and the residual atmosphere (e.g. H_2, O_2) [17,20,22]. For instance, several studies [17,20] showed that sputtering with a H-containing gas is detrimental for the S/W ratio due to H contamination through the $H + S \rightarrow H_2S$ reaction. In comparison, it was also reported that a sulfur deficit can be compensated by using an Ar-H_2S sputtering atmosphere. For instance, stoichiometric TMD layers or layers with excess sulfur can be achieved by reactive sputtering a MeY_2 or Me target with a fairly low HS_2 pressure [23,24] or sulfurization of MO_3 films in an H_2S atmosphere [25].

* Corresponding author.
E-mail address: y.pei@rug.nl (Y. Pei).

https://doi.org/10.1016/j.surfcoat.2018.04.040
Received 25 February 2018; Received in revised form 9 April 2018; Accepted 14 April 2018
Available online 17 April 2018

It has been well established [26–28] that the sputter-deposition parameters influence the stoichiometry, microstructure and mechanical properties of TMD tribocoatings. However, previous studies have not examined the influence of target-substrate distance in much detail. The present study concentrates on the effect of target-substrate distance on the microstructure, composition, stoichiometry, mechanical and tribological performance of $WS_xC(H)$ coatings deposited by either a reactive or a co-sputtering process.

2. Experimental details

2.1. Preparation of the $WS_xC(H)$ coatings

All $WS_xC(H)$ coatings were deposited on single crystal silicon(100) wafers. The substrates were first ultrasonically cleaned in acetone followed by Ar plasma etching for 20 min at pulsed direct current (p-DC) with −400 V bias voltage at 250 kHz and 87.5% duty cycle. The PVD power units for sputtering were operated in a current-control mode. A current of 0.5A was applied to two WS_2 targets (p-DC) at 150 kHz pulse frequency (62.5% duty cycle). For reactive sputtering of WS_xCH coatings, two different gas flow ratios, namely $Ar:C_2H_2$ = 15:10 sccm (referred to group S1 hereafter) and $Ar:C_2H_2$ = 20:5 sccm (referred to group S2 hereafter) were used to alter the carbon content. The unhydrogenated WS_xC coatings were deposited by co-sputtering two WS_2 targets and one graphite target (DC) in pure Ar atmosphere (25 sccm, referred to group S3 hereafter). To study the effect of the target-substrate distance on the S/W stoichiometry, microstructure and tribo-performance, each group of coatings was deposited at 70, 145, 220 and 290 mm distance away from the targets. This combination leads to a total of 12 coatings with different compositions. The coatings are hereafter referred to as Sx-Dy, with Sx (x = 1, 2, 3) indicating the flow rate of C_2H_2 gas (10, 5, 0 sccm) and Dy (y = 70, 145, 220, 290 mm) indicating the target-substrate distance in the deposition. As an example, S1-D70 refers to the coating deposited at a target-substrate distance of 70 mm by reactive sputtering with $Ar:C_2H_2$ = 15:10 sccm. A 25 sccm gas flow rate corresponds to a total pressure of around 0.6 Pa. A pure Cr (99.9%) target was powered by a Pinnacle 6/6 kW DC power to produce a Cr interlayer for enhancing coating interfacial adhesion. The coating deposition time was kept at 2 h for all samples. The substrates were self-biased using a floating potential. The base pressure of the chamber before deposition was 3–5 × 10^{-4} Pa. The substrates were mounted vertically on a carousel that was rotated at 3 rpm in front of the targets. No additional substrate heating was applied during deposition.

2.2. Characterization of the $WS_xC(H)$coatings

The microstructure was investigated using an environmental scanning electron microscope (ESEM, FEI FEG-XL30) and a high resolution transmission electron microscope (HRTEM, 2010F-JEOL). Energy dispersive X-ray spectroscopy (EDS, EDAX Octane Silicon Drift Detector) with an accelerating voltage of 20 kV in FEI XL30 ESEM was employed to determine the chemical composition of the coatings. Note that EDS results are averaged by accumulating the signal from the same size spot for 100 s on three random areas of each sample, with an error of 1 at.%. The grazing incidence X-ray diffraction (GIXRD) spectra were collected with a PANalytical-X'Pert MRD to determine the crystalline phases of the coatings using a 2° incident angle in parallel beam geometry. X-ray photoelectron spectroscopy (XPS) was performed to investigate the elemental composition and possible chemical bonding of the fresh coatings, using a Surface Science SSX-100 ESCA instrument with a monochromatic Al *Kα* X-ray source (hυ = 1486.6 eV). During data acquisition, the pressure in the measurement chamber was kept below 2 × 10^{-7} Pa. The electron takeoff angle with respect to the surface normal was 37° and the diameter of the analyzed area was 1000 μm and the total experimental energy resolution was set to 1.16 eV. The XPS spectra were analyzed using the least-squares curve fitting program (Winspec, developed at the LISE laboratory of the Faculte's Universitaires Notre-Dame de la Paix, Namur, Belgium). Binding energy was reported to ± 0.1 eV [29]. The hardness and elastic modulus of the composite coatings were measured by a MTS Nano indenter XP® equipped with a diamond Berkovich tip. The indentation depth was fixed at 150 nm, i.e. about 10% of the coating thickness, to avoid the influence of the substrate. Raman spectra on the wear tracks were acquired by Thorlabs HNL equipped with a HeNe laser (532 nm), at approximately 2.5 mW in the range 200–2000 cm^{-1}. The tribological properties of the coatings were investigated at room temperature using a ball-on-disk CSM tribometer, with a 100Cr6 steel ball (6 mm in diameter) at a sliding speed of 10 cm/s. The ball slides against the coating under a normal load of 5 N, resulting in a Hertz contact pressure of about 0.75 GPa. All samples were tribotested in both dry air (relative humidity of 5%, R_H) and in humid air (55% R_H) respectively, modulated by a home-made humidity adjustor. All wear tests were repeated twice for 10,000 laps unless catastrophic failure occurred. After the wear tests, the wear tracks of the coatings and the wear scars of the ball counterparts were characterized by an optical microscope. 3D confocal micrographs of the wear tracks were captured to measure the wear volume in order to evaluate the wear rates (W_r). Normalized wear rates ($mm^3 N^{-1} m^{-1}$) were then calculated through a Matlab code according to the following equation: K = V/(L × N), where V is the wear volume, L the total running distance of the ball over the disk, and N the normal load. To unveil the self-lubrication mechanism, a focused ion beam (FIB, Lyra Tescan, Czech) was applied to prepare lamellae in-situ on the wear tracks for cross-sectional TEM analysis.

3. Results and discussions

3.1. Chemical composition and structural characterization

3.1.1. Elemental composition

Fig. 1a shows that the chemical composition of sputtered $WS_xC(H)$ coatings changes upon target-substrate distance from 70 mm to 290 mm. EDS results inform on the atomic percentage of W, S, O and C excluding H, and EDS area mappings (not shown) indicated compositional homogeneity over the entire coating samples. As can be seen, the S1 group of coatings deposited with a high C_2H_2 flow rate have a high carbon content up to 60–70 at.% C, while the S2 and S3 coatings have a rather low C content of 16–27 at.%. Due to residual oxygen in the PVD chamber, around 1–6 at.% oxygen is incorporated in the coatings and the higher oxygen content corresponds to the longer target-substrate distances. Increasing the target-substrate distance leads to a remarkable increase in S content and a decrease in W content for S2 and S3 coatings, while in the coating S1 the S content does not change much, but the W content decreases significantly. Fig. 1b shows the S/W ratio as a function of the target-substrate distance for the three types of coatings. S/W is seen to increase almost linearly with target-substrate distance, i.e. from 0.51 in S3-D70 to 1.89 in S1-D290. At the shortest target-substrate distance of 70 mm, the hydrogenated S1 and S2 coatings both show a higher S/W ratio than the unhydrogenated coating S3. Similar results have been reported for WSeC coatings [20], where WSe_2 deposited by reactive sputtering in CH_4 atmosphere showed a much higher Se/W ratio than that co-sputtered with a graphite target. Dimigen [26] and Goeke [30] pointed out that plasma decomposition of H_2S even provides a controllable amount of sulfur to the growing film and allows to mitigate substoichiometry.

By combining Monte Carlo simulations and experiments to investigate the compositional variations of sputtered WS_2, Sarhmmar *et al.* [21] proposed that the S/W ratio varies significantly with the processing pressure as well as with the position of substrates relative to the targets because of the different scattering behaviors of S and W in the gas phase. Indeed, the processing pressure determines the mean free path of the species and thus changes the frequency of scattering and

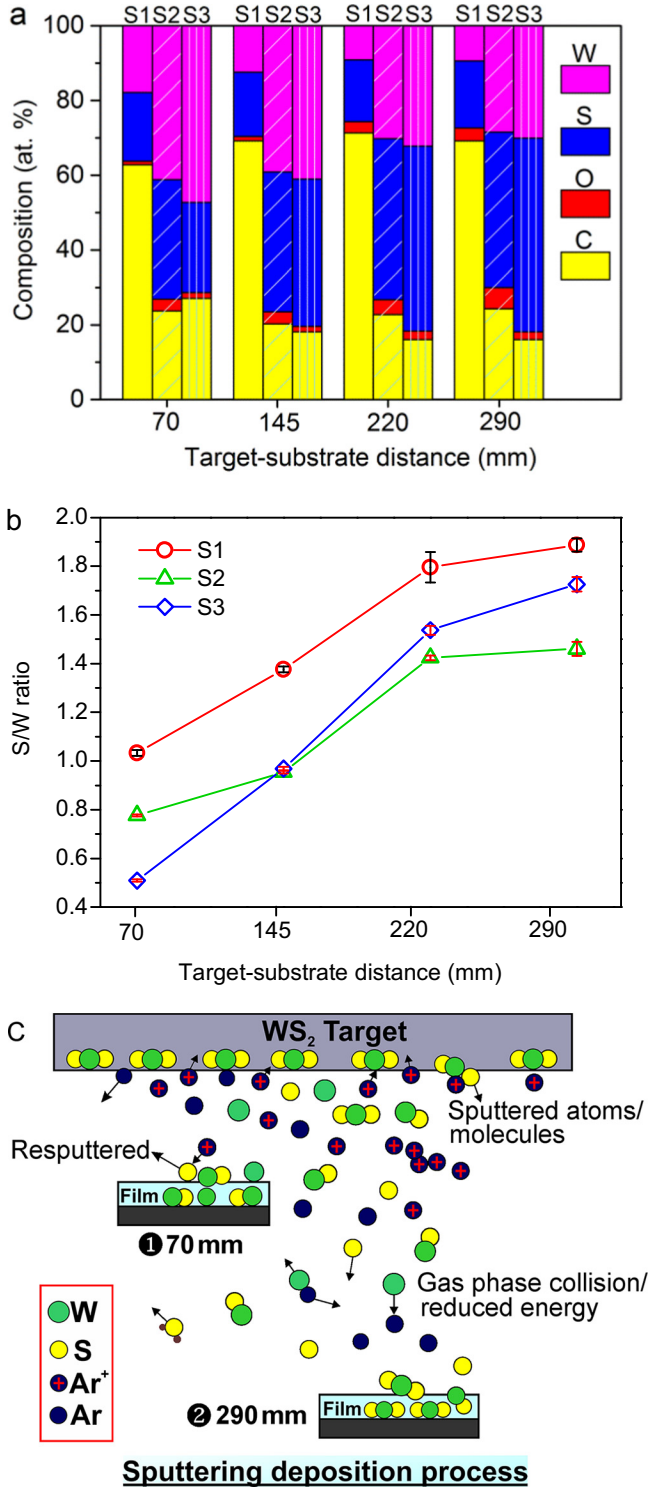

Fig. 1. (a) Atomic composition of each coating indicated; (b) increasing S/W ratio with increasing target-substrate distance; (c) schematic of sputtering deposition process. Note that H is excluded for compositional analysis.

collisions, thereby controlling the energy delivered to the growing coatings [21,26,31] by the impinging atoms/ions. A lower pressure yields substantial sulfur resputtering (low S/W ratio) due to enhanced energetic particle bombardment [32]. Since the total flow rate of gases in all the coatings investigated was kept at 25 sccm, the pressure can be estimated as being roughly the same. The deposition process is schematically depicted in Fig. 1c. The higher S/W ratio at larger target-substrate distance stems from more frequent collisions which lead to more scattering of large atoms such as W and to a reduction of the energy of the particles on their way to the substrate. Consequently less S resputtering of the growing film occurs. Such preferential resputtering was further confirmed by applying a bias substrate voltage of −50 V for coating S3-D70, which significantly decreased the S/W ratio from 0.51 to almost zero (not shown), in agreement with Ref. [33]. Conversely, for a WS_x/a-C multilayer film a higher a-C/WS_x thickness ratio generates a higher S/W ratio because the a-C layer on top of the WS_x layer prevents the latter from being bombarded and hence from loosing sulfur [34].

According to Ref. [35], momentum and energy are transferred in the collisions from the moving particles (Ar species) to the stationary target atoms (deposited W, S on the substrate). The reduction in energy relies on the masses of incident and target atoms. Assuming a scattering angle of $\theta = 180^\circ$, the energy transfer ratio is $K = \frac{4\,M1M2}{(M1+M2)^2}$, where M1 and M2 refer to the mass of energetic incident and rest target atoms, respectively. When the masses are identical, K equals unity and the larger mass difference, the lower K will be. The atomic masses of Ar, S and W atom are 40, 32 and 184 respectively, so that the light S atoms (close to Ar) deposited on the substrate are more easily resputtered than W atoms. Also, S has a high vapor pressure (e.g. $\sim 3 \times 10^{-4}$ Pa at room temperature) [30] and binds weakly to the substrate. On the other hand, the heavier W atoms cannot move far from the target after being sputtered, and this also accounts for the higher content of W in the coatings deposited at shorter target-substrate distances and the enrichment of S in the coatings deposited at longer target-substrate distances. It should be stressed that the target-substrate distance, negative bias voltage, deposition pressure (determining the mean free path of the species) and large S—W atomic mass difference all matter in determining S/W ratio of $WS_xC(H)$ coatings.

3.1.2. *Microstructure and crystallinity*

Fig. 2a-f present the SEM images of S1-S3 $WS_xC(H)$ coatings deposited at the target-substrate distance of 70 and 290 mm, respectively. The $WS_xC(H)$ coatings were found to be structurally similar to the typical cauliflower-like PVD sputtered DLC coatings. The insets of Fig. 2a-c present the corresponding fractured cross-section images, which clearly indicate that the coatings deposited at a target-substrate distance of 70 mm, whether by cosputtering or reactive sputtering, exhibit a dense and featureless microstructure. In contrast, the insets of Fig. 2d-f show that $WS_xC(H)$ coatings deposited at a target-substrate distance of 290 mm become less compact and present columnar-like structures. HRTEM images presented in Fig. 2g and h show that the reactively sputtered coatings S1 and S2 both present a quasi-amorphous structure, although some short WS_2 platelets are apparent in the S-rich coating S2-D290. The HRTEM image of the nonreactive sputtered coating S3-D290 presented in Fig. 2i exhibits dense nanocrystalline WS_2 platelets of 10 nm length, randomly incorporated in an amorphous carbon matrix.

Fig. 3 shows the GIXRD patterns of the $WS_xC(H)$ coatings. The patterns are similar; each coating is characterized by an asymmetrical (100) peak (edge plane) around $2\theta = 33^\circ$ with a long tail. This is generally ascribed to the effect of the turbostratic stacking of WS_2 basal planes with other planes. Weise *et al.* [27] reported that the referred XRD patterns of TMD point to a two-dimensional (2D) organization of the basal planes with several tens of unit cells. The stacking in the c-direction of the a-b basal lattice planes with lateral dimensions in the range of a few nanometers, results in a sharp peak at approximately the position for the (100) reflections. The peak tails towards larger angles suggesting other reflections of the (10*Z*) family with Z = 1, 2, 3… [27,31] and consequently presenting broader peaks typically of an amorphous structure.

Since the most important diffraction pattern of (002) basal plane is usually absent in the reported XRD spectra of TMDs [36–39], it is crucial to mention that provided the target-substrate distance is beyond 145 mm, a (002) peak of WS_2 was detected in S3 coatings. The

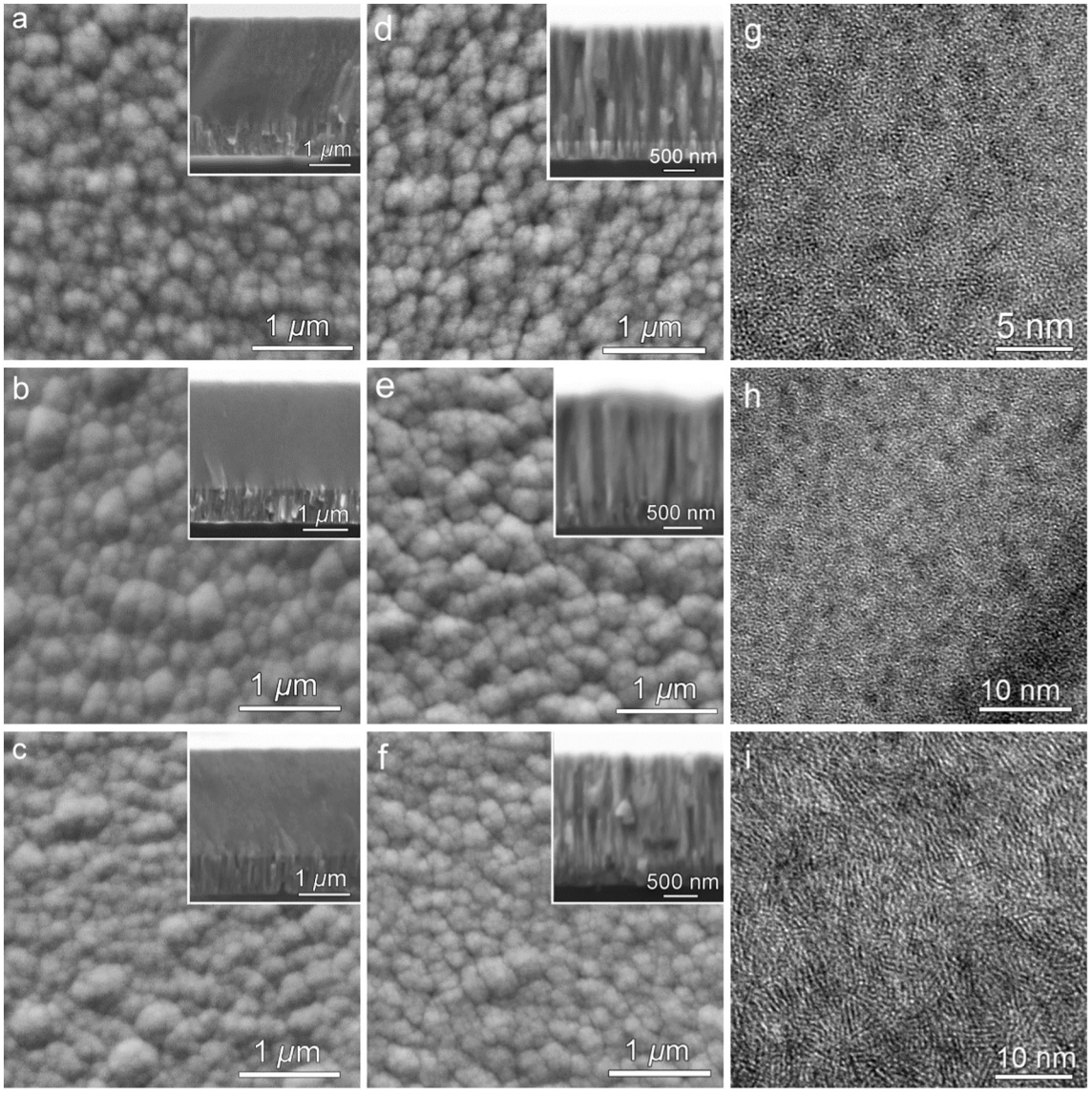

Fig. 2. (a-c) S1-S3 coatings deposited at a target-substrate distance of D = 70 mm; (d-f) S1-S3 coatings deposited at D = 290 mm; (g-i) HRTEM images of (d-f) respectively.

comparisons of WS_xC with a pure sputtered WS_2 coating (see Ref. [32]) evidences a slight shift of the (002) peak towards lower diffraction angles from (~ 14° to 12°) when WS_2 is doped with carbon because carbon incorporation increases the lattice parameters of WS_2 [37]. A similar lattice expansion was also reported in Ti-WS_2 coatings [40]. The strong (002) reflection indicates that some WS_2 crystals are oriented with their basal planes parallel to the surface, which is typical for a type II structure of sputtered TMD coatings [1]. The basal plane orientation of WS_2 plays a vital role in various applications including tribo-fields (minimum friction, strong adhesion to substrate and inertness to oxidations) [41] and even in thin film solar cells (high absorption coefficient) [23]. Numerous strategies such as pressure control [32], doping with Ni [12], deposition temperature [23] and different atmospheres [26] were exploited to realize films with well aligned basal planes. This study indicates that a larger target-substrate distance may offer an alternative route to achieve the desired orientation of the basal planes in WS_2 films. Besides, Cr diffraction peaks arise from the interlayer (see Fig. 3a and b).

3.1.3. Chemical bonding

The chemical bonds of the $WS_xC(H)$ composite coatings deposited at D = 290 mm were characterized by XPS spectra, as shown in Fig. 4. As an example, S3-D70 coating was also analyzed for comparisons. To avoid possible sputter damages such as sulfur resputtering and chemical state variations [42], no preliminary Ar etching process on as-deposited coatings was applied. Fig. 4a shows the survey scans, where the W4f, S2p, C1s and O1s peaks are evident for all coatings. However, the intensity of the C1s peak is more prominent in coating S1-D290, while the O1s peak is less intense in coating S3-D70, in agreement with the EDS data discussed earlier.

The C1s peaks at a binding energy (BE) of 284.5 eV [43] corresponds to amorphous carbon. The detailed S2p and W4f spectra are shown in Fig. 4b and c. The S2p doublets with maxima at 161.8 eV and about 163.6 eV correspond to S—W and S—C bonds [34,37,43,44]; the latter are probably located at the interface between the WS_2 and the amorphous carbon. In particular, the intensity of S—C bonds contributes as much as 46.7% to the total S signal for the high-carbon coating S1-D290.

The deconvolution of the $W4f_{7/2}$ spectra (Fig. 4c) demonstrates the presence of W—S and W—O bonds at BEs of 32.9 eV and 35.6 eV, respectively, which can be ascribed to WS_2 and WO_3 [37,42,43,45]. The third $W4f_{7/2}$ contribution situated at a BE of around 32.1 eV [37]

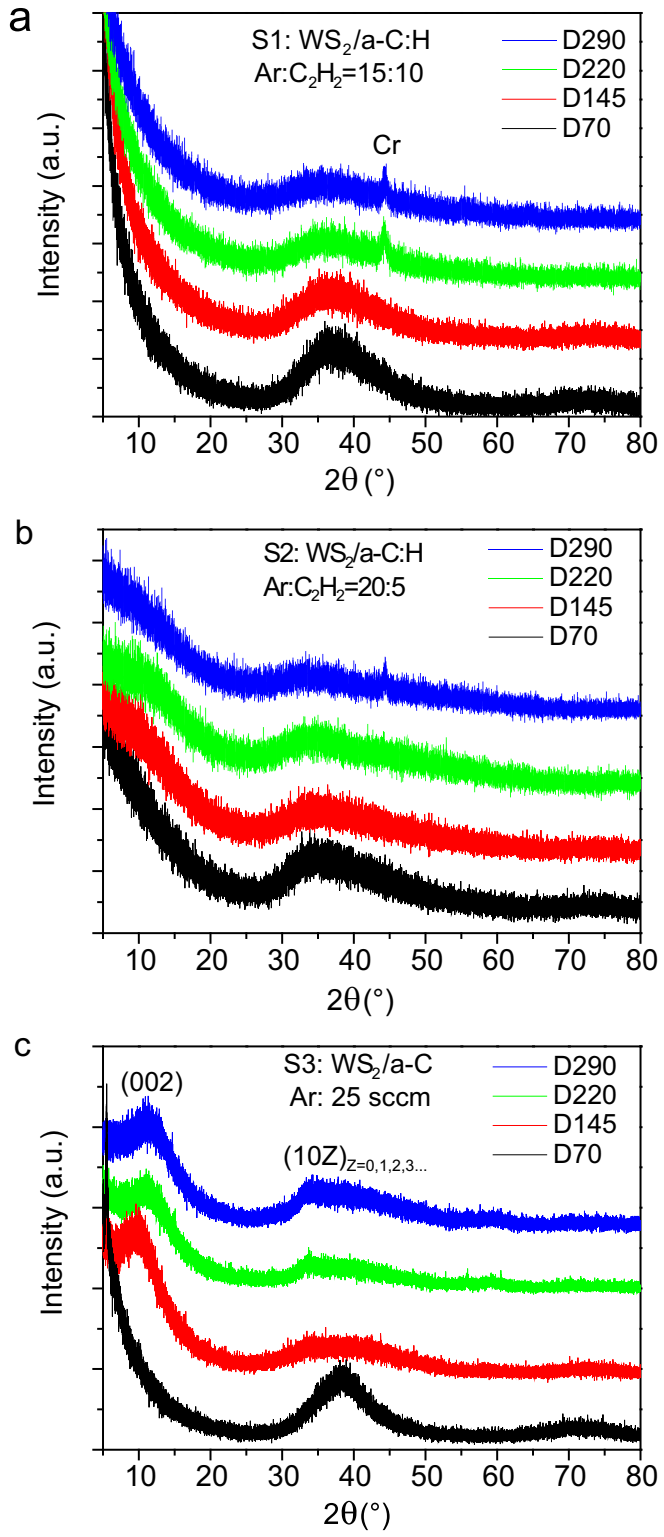

Fig. 3. GIXRD spectra for coatings under different target-substrate distances: (a) S1; (b) S2; (3) S3.

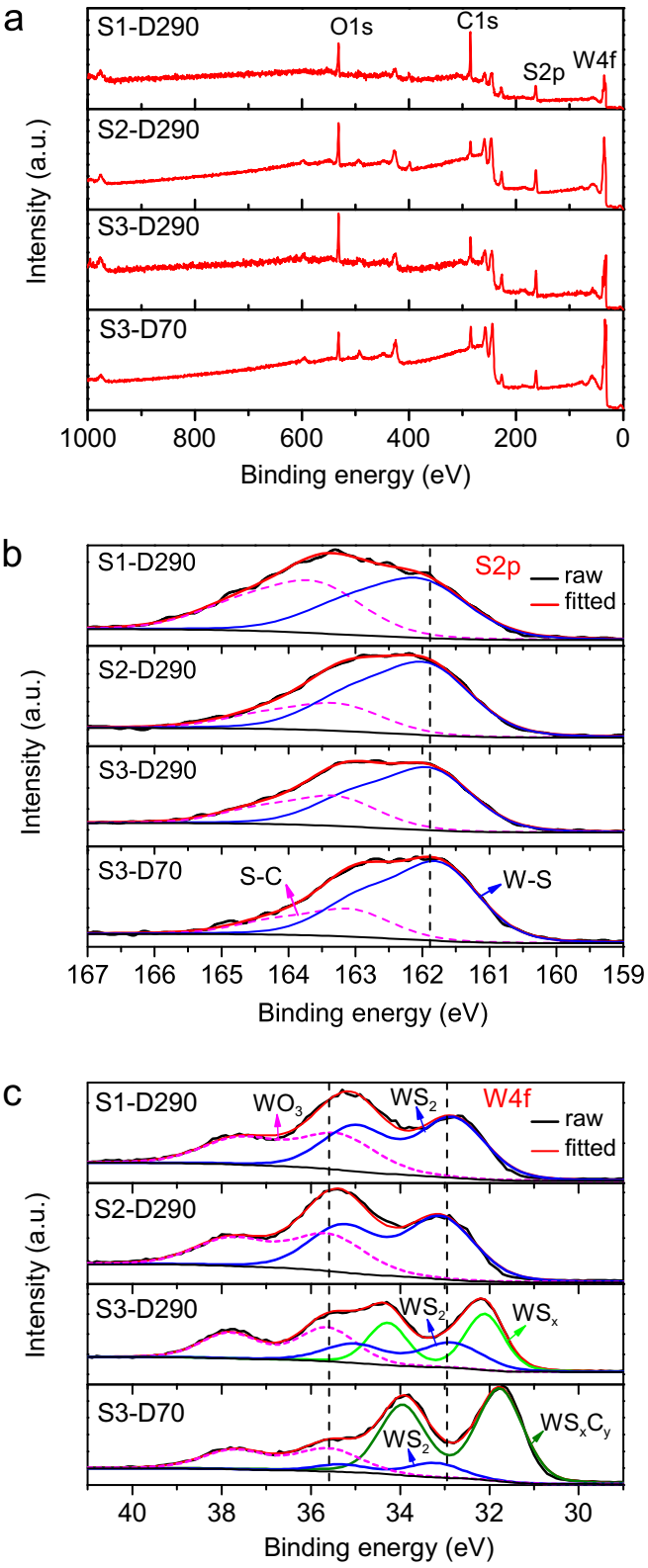

Fig. 4. XPS spectra of the coatings deposited at various conditions: (a) survey scan; (b) high resolution scan of C1s spectra; (2) high resolution scan of S2p spectra; (3) high resolution scan of W4f spectra. Note that the spectra are the averaged value of three measurements for each test.

present for the coating S3-D290 is attributed to WS_x ($x < 2$). Another lower BE component at 31.7 eV in the spectrum of the coating S3-D70 stems from W−C bonds [37,43,45]. Coatings S3-(D70, D290) should have close chemical state since they are both deposited by cosputtering, thus WC in coating S3-D70 is supposed to mingle with WS_x and it is probably more suitable to ascribe this component to an intermediate mixture of WS_xC_y, similar to the reported TiS_xC_y [37]. In addition, Ar^+ bombardment can induce reduction of W in high valence states [45,46], e.g. $W(6^+)$ to W (0) and the sulfur preferential lost from the surface also enriches the surface in metallic W. The coating S3-D70, produced under the strongest Ar^+ bombardment, is highly rich in tungsten (47.3 at.%),

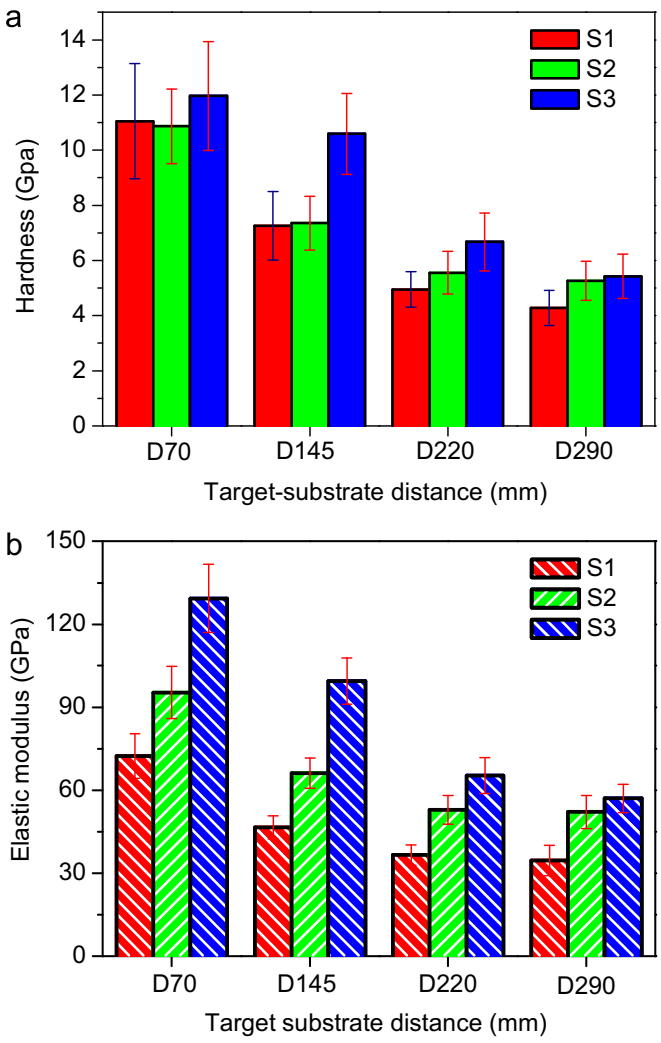

Fig. 5. (a) Hardness and (b) elastic modulus of all tested coatings.

so the low-BE component at 31.4 eV [45,47] presumably contains a contribution from metallic W. This is also supported by a broader FWHM of 1.2 eV as compared to 1.0 eV for coating S3-D290. However, it is difficult to separate the contribution of WC from that of metallic W because their BEs are close. Note that WO_3 may mainly arise from surface oxides since W−O bonds can be remarkably reduced after ion sputter etching [37,42,45]. This can be reconfirmed by the lowest WO_3 contribution in the coating S3-D70: the heavy bombardment under which this coating was produced, diminishes the number of active sites for oxidization at the expense of a sufficient amount of S (S/W = 0.51). Although no clear W−C peaks are detected in the XRD (see Fig. 3), we cannot rule out the possibility that WC is amorphous and randomly distributed in the matrix [37,44].

3.2. Mechanical properties

Fig. 5 shows the average hardness (H) and elastic modulus (E) of all the $WS_xC(H)$ coatings. First, a significant decrease in hardness was observed with increasing target-substrate distance from 70 to 220 mm but then remains nearly unchanged on going from 220 to 290 mm. The nonreactive coating was found to have an overall higher hardness, from ~ 12.0 GPa at D = 70 mm to 5.4 GPa at D = 290 mm. The hardness of S1 and S2 coatings showed a similar trend with a decrease from 11.0 GPa to 4.3 GPa. It should be pointed out that compared with the pure sputtered WS_2 coatings with hardness < 1 GPa [18,32], above one order of magnitude higher hardness can be attained by the incorporation of moderate amounts of carbon into WS_2. Carbon addition enhances the compactness of the coating and facilitates possible formation of strong W−C bonds as discussed for the XPS results of coating S3-D70 [37]. Our earlier results [32] showed that the hardness of WS_2/a-C coating increases with increasing carbon content up to ~40 at.%, reaching a maximum of 10.6 GPa, but then levels out or even decreases upon further higher carbon content. As discussed in Fig. 1a, S1 has a relatively high carbon content as compared to S2 and S3 (~ 70 at.% vs. 20 at.%), but its hardness is even slightly lower than that of the latter. In fact, these major hardness variations can again be explained by the effect of Ar bombardment: the S3 coatings were deposited a pure Ar atmosphere with the highest flux (25 sccm) yielding the strongest bombardment with energetic particles. This indirectly explains why coatings deposited at shorter target-substrate distances present a higher hardness. The decreased Ar flow rate from 20 sccm (S2) to 15 sccm (S1) reduces the hardness.

The variations in elastic moduli, shown in Fig. 5b, closely track the hardness variations, with the highest elastic modulus of 129.4 GPa measured for coating S3-D70 and the lowest of only 34.6 GPa for coating S1-D290. According to the Leyland's findings [48], high H/E ratio is commonly regarded as a reliable indicator of better wear resistance for DLC-based coatings. The H/E ratio of the $WS_xC(H)$ coatings tends to decrease with increasing target-substrate distance for S1 and S2. For instance, the H/E of S1 coatings equals to 0.15, 0.16, 0.13 and 0.12 respectively, as the target-substrate distance increases from 70 mm to 290 mm. While the H/E ratio for S1 is slightly higher than S2, S3 almost has the same H/E values of ~ 0.1. To conclude, a shorter target-substrate distance leads to microstructure densification, which potentially enhances the wear resistance.

3.3. Tribological properties

3.3.1. Friction and wear

Pin-on-disk wear tests were performed under dry air (5% R_H) and humid air (55% R_H). Fig. 6a and b show the mean CoF for all the tribotests over 10,000 sliding laps, whereas Fig. 6c and d show the wear rate (W_r). Fig. 6e and f display the instant CoFs of the coatings deposited at a target-substrate distance of 70 mm and 290 mm, respectively. Fig.7 presents the morphologies of wear tracks and corresponding counterpart scars. For sliding in dry air, the behavior of coating S3-D70 showing a high CoF of 0.26 ± 0.08 with large deviations, is remarkably different from that of the other coatings which exhibit relatively low CoFs. In particular, minimum values of 0.023 ± 0.02 and 0.024 ± 0.02 are measured for the coating S3-D220 and S3-D290. In fact, CoFs of the coatings S2 and S3 with similar content of carbon (~20 at.%) slightly decrease with higher S/W ratio that results at larger target-substrate distance. On the contrary, the CoFs of high-carbon S1 coatings present an upward trend with target-substrate distance, with a lowest value of 0.053 for the coating produced at D = 70 mm and the highest CoF of 0.114 for the one deposited at D = 290 mm. The wear rates, W_r, are depicted in Fig. 6c. A strikingly high W_r of 4.14×10^{-6} $mm^3 N^{-1} m^{-1}$ stands out for coating S3-D70, while the wear rates of the other coatings are all one order of magnitude lower, reaching down to a W_r of 1.4×10^{-7} $mm^3 N^{-1} m^{-1}$ for coating S3-D145. In general, W_r increases with increasing target-substrate distance. Overall the higher H/E ratio may account for the lower W_r of S1 as compared to S2, considering that both are hydrogenated coatings with comparable hardness, as indicated in Fig. 5a.

For tribotests in humid air of 55% R_H, the CoFs of the cosputtered S3 coatings are much lower than those of the reactively sputtered S1 and S2 coatings. The CoFs of S3 coatings in humid air remain in the range of 0.10–0.13 - except for S3-D70, where its CoF reaches 0.023, while the CoFs of high-carbon coatings S1 range between 0.22 and 0.27. The CoFs of S2 coatings are surprisingly high, increasing from 0.48 to 0.80 with increasing target-substrate distance. This reveals a coating failure as a CoF > 0.6 is usually regarded as an indicator of direct metal contact

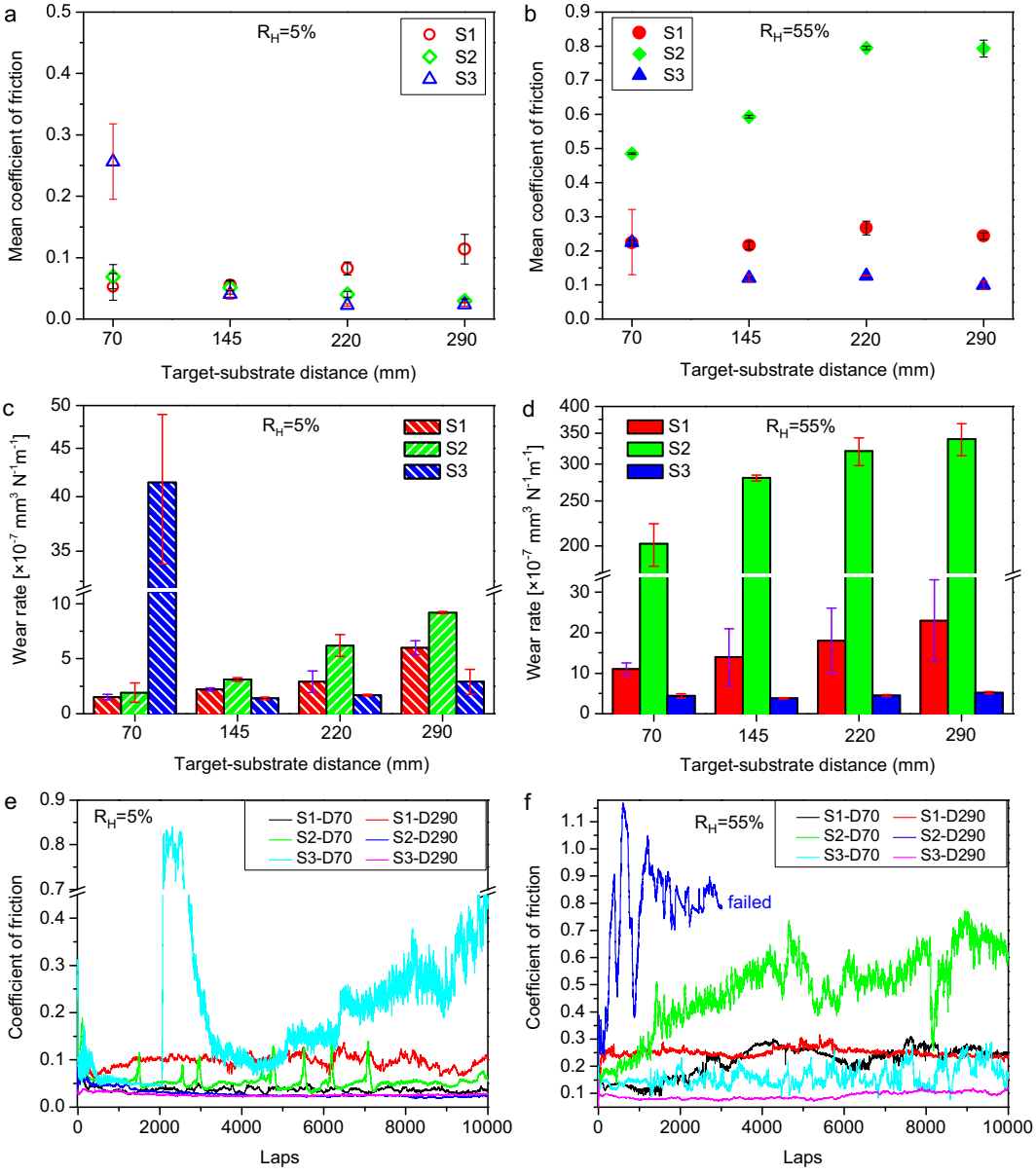

Fig. 6. Coefficient of friction (CoF) and wear rate (W_r) of $WS_xC(H)$ coatings under differentt target-substrate distances: (a, b) average CoF; (c, d) W_r; (e, f) typical CoFs of coatings desposited at D = 70 and D = 290 mm, respectively (5 N load).

[49]. This deterioration is confirmed by the high W_r coming into the range of $10^{-5}\,mm^3\,N^{-1}\,m^{-1}$ as shown in Fig. 6d. Similarly, the W_r of S1 coatings increases from $1.1 \times 10^{-6}\,mm^3\,N^{-1}\,m^{-1}$ to $2.3 \times 10^{-6}\,mm^3\,N^{-1}\,m^{-1}$, which is still higher than that of S3 coatings where the wear rate remains in the range $3.8–5.2 \times 10^{-7}\,mm^3\,N^{-1}\,m^{-1}$.

A closer look at Fig. 6e reveals that for coating S3-D70, the CoF in dry air shows great fluctuations. In fact it starts from 0.4 and decreases to 0.05 after sliding 1000 laps; after sliding for 2000 laps the CoF increases to 0.8, followed by leveling off at about 0.1 and rebounding to 0.4 at 10000 laps ultimately. In contrast, S3-D290 exhibits an initial ultralow CoF of 0.026, which remains rather constant (0.02) during the entire test and the same coating tested in humid air has a CoF which stabilizes rapidly at 0.10 (see Fig. 6f). (*S1*, *S2*)-D290 respond instead much more negatively to the presence of humidity. An immediate rise of CoF to 1.1 manifests an rapid catastrophic failure for S2-D290 in humid air. Fig. 7 (a, b, e, f, i, j) confirm comparable wear scar/track widths (~ 140 μm) of all coatings in dry sliding. The transfer layers densely cover the whole wear scars and leave debris behind. Substantial adhesive tribolayers are formed in the wear track of the S3-D290 (see the dark areas in Fig. 7j). While only S3-D290 coating survives intact in humid air, S1-D290 suffers from partial coating delaminations (see Fig. 7d) and the huge wear width up to 750 μm (see Fig. 7g and h) confirms a total failure for coating S2-D290.

It can be concluded that no matter whether in dry or humid air, the S3 coatings outperform the S1 and S2 coatings in terms of low CoF and W_r, provided that they were produced at target-substrate distances above 145 mm. This indicates intrinsically different lubrication mechanisms for the $WS_xC(H)$ nanocomposite coatings with varied S content. The triboperformance is also influenced by the type of sputtering process used to fabricate the coating. Hydrogenated and non-hydrogenated DLC-based coatings tribologically behave differently in that hydrogenated coatings exhibit ultralow friction in dry air while the non-hydrogenated coatings perform better in humid atmosphere [50].

Fig. 8 shows the Raman spectra on the wear tracks of the coatings deposited at D = 290 mm. For dry air sliding, Fig. 8a indicates the high-carbon S1 coating (70.0 at.% C) shows Raman-active bands exclusively in the 1300–1600 cm^{-1} region, corresponding to the typical D

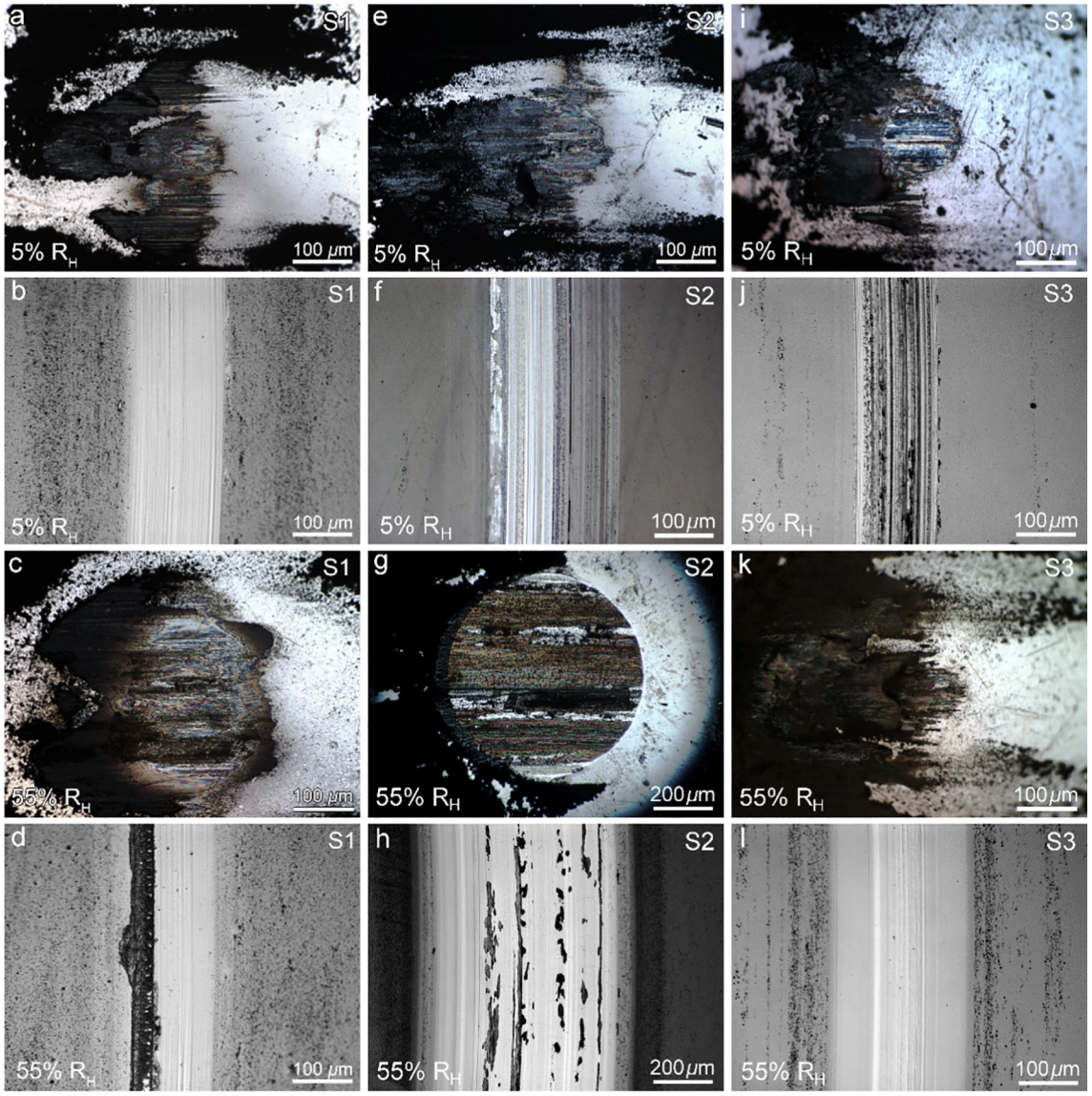

Fig. 7. Optical micrographs of wear scars of 100 Cr6 steel ball counterpart and wear tracks of $WS_xC(H)$ coatings (D = 290 mm) tested in dry air (R_H = 5%) and humid air (R_H = 55%): (a-d) S1-D290; (e-h) S2-D290; (i-l) S3-D290.

(~ 1360 cm^{-1}) and G (~ 1565 cm^{-1}) peaks of amorphous carbon; this indicates that the hydrogenated DLC matrix contributes a low-friction tribological behavior. The WS_2 peaks E^1_{2g} (~ 355 cm^{-1}) and A_{1g} (421 cm^{-1}) characteristic of hexagonal WS_2 [40] appear in coating S2-D290. For this coating, the rapid reduction of CoF from 0.11 to 0.03 at the onset of sliding suggests that WS_2 starts to perform. This can be further confirmed by the Raman spectrum of the S-richer S3 coating (51.8 at.% S), where intense WS_2 peaks appear and correlate with a lower CoF (0.024). Such an ultralow CoF is rarely reported for the nonhydrogenated DLC in dry air, which normally has a CoF above 0.1 before graphitization [6]. The ultralow CoF is thus predominantly attributed to the lubricating effect of the WS_2 phase.

Fig. 8b shows that only the D and G bands were measured on the wear tracks of S1-D290 pointing to the fact that the CoF of 0.25, a value commonly measured for the hydrogenated DLC in humid air, is primarily determined by the DLC matrix [50]. Note that for the S2 coating where, as discussed previously (Fig. 6f and Fig. 7g and h), catastrophic failure occurred, the weak D and G peaks and the small signal from WS_2 in the Raman spectrum in Fig. 8b probably arise from the very thin residual film on the damaged wear tracks (see Fig. 7h). The S3-D290 coating, whose low CoF of ~ 0.10 in humid air was attributed to both DLC and richness in WS_2, shows a Raman fingerprint with stretching bonds of WO_3 at 700–810 cm^{-1} [19] testifying to oxidation. The latter was probably produced mostly by reactions of WS_2 with H_2O from the humid air. Previous results [51] have suggested that only absorbed water attacks dangling bonds at WS_2 edge sites or defects, leading to larger lamellar attractions and thus higher shear strength. Correspondingly a higher CoF results and thus thicker debris covering the ball as seen in Fig. 7k if compared to Fig.7i which depicts the dry sliding wear track.

There are contrasting results reported in the literature concerning the origin of the triboperformance of WS_2/a-C coating; in fact Voevodin and coworkers assign the chameleon behavior of this coating to the joint contribution of DLC and WS_2 [15,16], but recent results presented by Polcar *et al.* [38,52] suggested that only WS_2 phases provide lubrication whereas DLC improves the overall mechanical properties. This study suggests a potential contribution of DLC matrix in reducing CoF and in increasing the wear resistance. Indeed, although the presence of amorphous carbon in all wear tracks is confirmed by the Raman spectra, the (*S2*, *S3*)-D290 coatings of approximately same hardness and elastic modulus behave rather differently in tribo-performance, particularly in humid air (CoF: 0.8 vs. 0.10, and W_r:

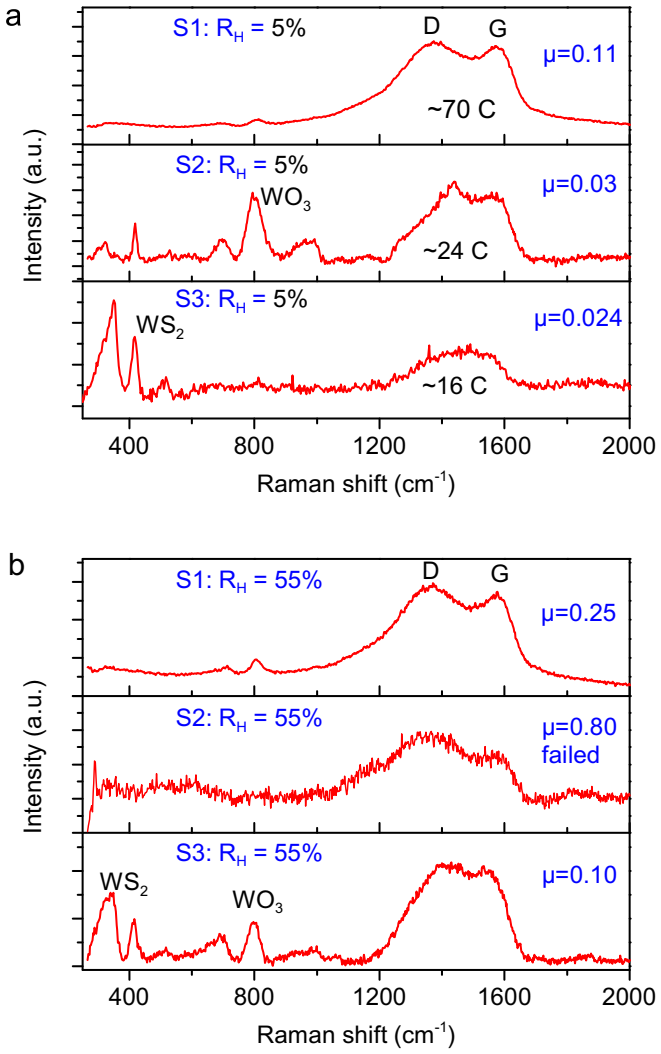

Fig. 8. Raman spectra of the wear tracks of $WS_xC(H)$ coatings deposited at D = 290 mm after sliding for 10,000 laps in different humidities: (a) R_H = 5% and (b) R_H = 55%.

10^{-5} mm^3 N^{-1} m^{-1} vs. 10^{-7} mm^3 N^{-1} m^{-1}). The lubrication of WS_2 in (*S2*, *S3*)-D290 coatings is comparable considering that their chemical composition is very similar (see Fig. 1a). This implies that the unhydrogenated DLC matrix at least partially plays a role as lubricant in humid air sliding. Earlier work [32] also reported C-rich WS_2/a-C coating presents much lower W_r in humid air sliding. However, further pertinent experiments and MD simulations are required to unravel the underlying mechanism for this behavior.

Notably, to achieve an ultralow friction it is not necessary to reach the stoichiometric WS_2 in the $WS_xC(H)$ coatings. A clear correlation can be found between the S/W ratio (Fig. 1b) and the CoF (Fig. 6a and b), displaying values below 0.05 (in dry air) and around 0.10 (in ambient air) for ratios S/W ≥ 0.95, provided the target-substrate distance exceeds 145 mm. A threshold value of Se/W ≥ 0.6 was also found in WSeC to be sufficient to reduce the CoF below 0.1 even in ambient air and no further reduction occurred for Se/W > 1 [39]. Our earlier work [32] demonstrated stable ultralow CoFs in the level of 0.02, almost independently of the S/W ratio in the range S/W = 1.33–1.79. Yet contrasting with Ref. [53], where MoS_2/a-C coatings with low sulfur content (< 10 at. %) and ultralow (Mo + S)/C ratio (0.04–0.19) could produce low CoFs in diverse environments (air, N_2, vacuum), this study indicates that besides the appropriate S/W ratio, a high total content of sulfur is equally crucial for an ultralow friction. For S1 coatings, all with < 20 at. % S content, show a higher CoF as compared to S2 coatings when sliding in dry air. Particularly for the W-rich S3-D70 coating, both the low S/W ratio (0.51) and low S total content result in unacceptable triboperformance (see Fig. 6). The low sulfur content makes it more difficult to reorient WS_2 platelets parallel to the wear interface or entails longer sliding time to do so [32]. Ref. [32] also reported a worse triboperformance for the S-poor WS_xC coating with a high S/W ratio (1.79). These results agree with the findings by Voevodin *et al.* [6] that WS_xC coatings with scarce sulfur content perform unsatisfactorily in dry conditions. It can be concluded that, for tribological applications, $WS_xC(H)$ coatings are not necessarily to reach WS_2 stoichiometry by excessively increasing the target-substrate distance, which potentially undermines the wear resistance due to significant reduction in hardness and compactness and also lowers the deposition rate (see Fig. 2).

3.3.2. *Characterization of the WS_2 tribofilm*

We chose coating S3-D290, which showed a good triboperformance with CoFs of ~ 0.02 and 0.10 in dry and humid air, respectively for post-test analysis by TEM. TEM cross-section lamella were prepared by focused ion beam slicing in the wear track, parallel to the sliding direction after 10,000 laps in dry air. Fig. 9a and b demonstrate that a thick tribofilm was formed during sliding and the TEM image in Fig. 9c shows the tribofilm can be up to 150 nm thick. HRTEM images (Fig. 9d-f) confirm that characteristic WS_2 platelets are formed and aligned parallel to the sliding interface. Notably, in the image in Fig. 9d one can distinguish the long (> tens of nm) WS_2 platelets formed in the tribofilm from the randomized short WS_2 platelets (5 nm) in the raw coating. Most interestingly, perfectly aligned lamellae, with d = 0.63 nm characteristic of (002) WS_2 plane, extend up to > 60 nm, which is much thicker than reported in earlier work (several nm) [37,54]. Fig. 9e shows that the lamellae become less realigned at the outmost surface of the tribofilm. Fig. 9d also shows the formation of few WO_3 nanocrystallites (circled dark areas) about 20 nm away from the interface, proving that well-ordered WS_2 on the top surface protects the coatings from oxidizing. Besides, the CoF of the S3-D290 coating immediately falls to the range of 0.02 and stabilizes during the whole sliding, suggesting the reorientation process continues throughout the whole wear lifetime.

4. Conclusions

$WS_xC(H)$ nanocomposite coatings were prepared either by reactive sputtering or nonreactive co-sputtering. This work mainly studied the effect of the target-substrate distance on the S/W stoichiometry, the microstructure and the structure-property relationship. The lubricating mechanisms were also discussed.

1) For $WS_xC(H)$ nanocomposite coatings, the S/W stoichiometric ratio increases with target-substrate distance. Randomly-oriented WS_2 platelets are observed in the co-sputtered S3-D290 coating. Preferential resputtering of sulfur reinforced by energetic particles impingement on the growing coating primarily accounts for the low S/W ratio.
2) The hardness and elastic modulus decrease with increasing distance between target and substrate and the co-sputtered S3 coatings show overall a higher hardness and larger elastic modulus than the reactively sputtered S1 and S2 coatings.
3) For dry air sliding (< 5% R_H), low CoFs could be reached in all $WS_xC(H)$ coatings except for coating S1-D70 characterized by both low S/W ratio and low S content. Co-sputtered WS_xC coatings are preferable for tribological applications in high humidity.
4) Cross-sectional TEM of tribofilms reveals that thick WS_2 platelets with basal planes aligned parallel to the sliding direction are generated during the frictional contact.

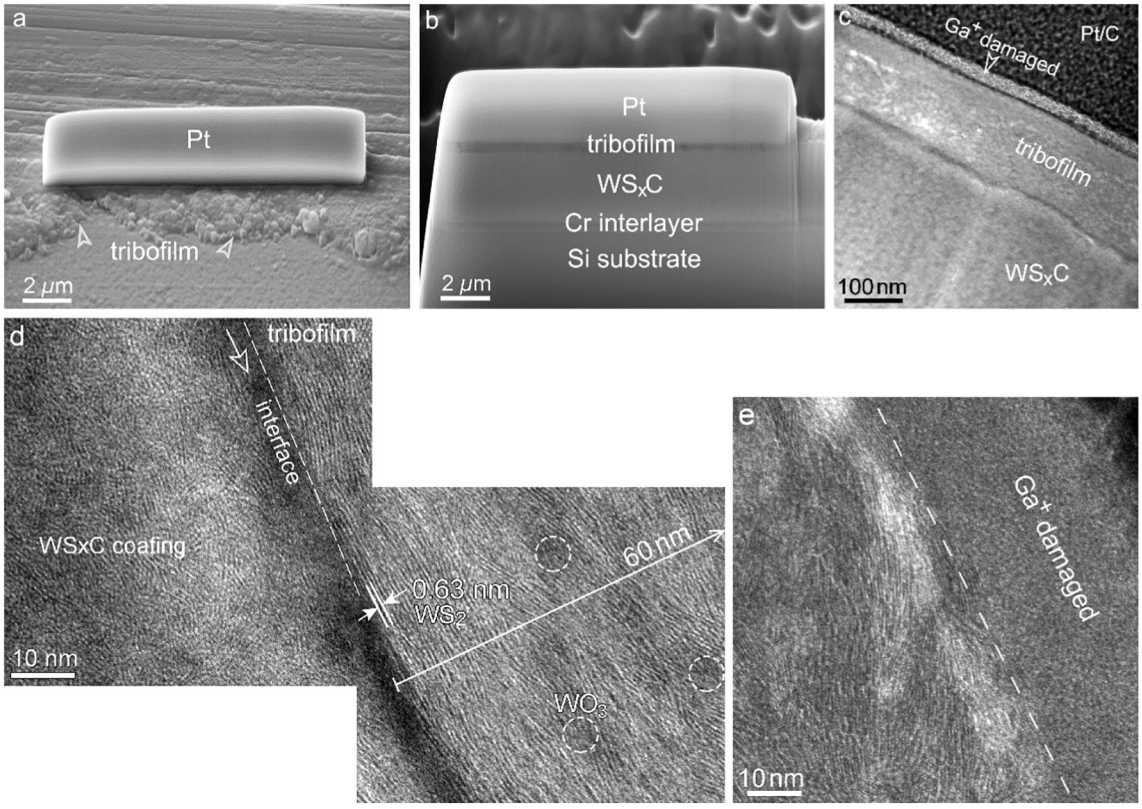

Fig. 9. TEM lamella by FIB-cut on the dry wear track (R_H = 5%) of coating S3-D290: (a) Pt protective layer; (b) cross-section of graded microstructure after FIB milling. (c) TEM image of the cross section from WS_xC coating to tribofilm; (d-e) HRTEM images elucidating that crystalline WS_2 basal planes were reoriented in the tribofilm along the sliding direction.

Acknowledgments

Huatang Cao acknowledges the China Scholarship Council (CSC, No. 201406160102) for his PhD Scholarship. The authors thank Mr. Mart Salverda and Professor Wesley Browne of University of Groningen for their help with the GIXRD and Raman measurements, respectively. Feng Wen from Hainan University, China, thanks for the grant of visiting scholar from the China Scholarship Council.

References

[1] C. Muratore, A.A. Voevodin, Annu. Rev. Mater. Res. 39 (2009) 297–324.
[2] P.D. Fleischauer, Thin Solid Films 154 (1987) 309–322.
[3] T. Spalvins, Thin Solid Films 118 (1984) 375–384.
[4] F. Gustavsson, S. Jacobson, A. Cavaleiro, T. Polcar, Surf. Coat. Technol. 232 (2013) 541–548.
[5] L. Isaeva, J. Sundberg, S. Mukherjee, C.J. Pelliccione, A. Lindblad, C.U. Segre, U. Jansson, D.D. Sarmac, O. Erikssona, K. Kádasae, Acta Mater. 82 (2015) 84–93.
[6] A.A. Voevodin, J.P. O'Neill, J.S. Zabinski, Surf. Coat. Technol. 116–119 (1999) 36–45.
[7] A.A. Voevodin, J.S. Zabinski, Compos. Sci. Technol. 65 (2005) 741–748.
[8] H. Li, X. Li, G.A. Zhang, L.P. Wang, G.Z. Wu, Tribol. Lett. 65 (2017) 1–10.
[9] P. Tomas, F. Gustavsson, T. Thersleff, S. Jacobson, A. Cavaleiro, Faraday Discuss. 156 (2012) 383–401.
[10] J.J. Nainaparampil, A.R. Phani, J.E. Krzanowski, J.S. Zabinski, Surf. Coat. Technol. 187 (2004) 326–335.
[11] S.M. Ren, H. Li, M.J. Cui, L.P. Wang, J.B. Pu, Appl. Surf. Sci. 401 (2017) 362–372.
[12] S.H. Xu, X.M. Gao, M. Hu, J.Y. Sun, D. Jiang, F. Zhou, W.M. Liu, L.J. Weng, Appl. Surf. Sci. 288 (2014) 15–25.
[13] S. Cai, P. Guo, J.Z. Liu, D. Zhang, P.L. Ke, A.Y. Wang, Y.J. Zhu, Tribol. Lett. 65 (2017) 79–90.
[14] M. Evaristo, T. Polcar, A. Cavaleiro, Int. J. Mech. Mater. Des. 4 (2008) 137–143.
[15] A.A. Voevodin, J.P. O'Neill, J.S. Zabinski, Tribol. Lett. 6 (1999) 75–78.
[16] A.A. Voevodin, J.S. Zabinski, Thin Solid Films 370 (2000) 223–231.
[17] T. Polcar, A. Nossa, M. Evaristo, A. Cavaleiro, Rev. Adv. Mater. Sci. 15 (2007) 118–126.
[18] J. Xu, L.Q. Chai, L. Qiao, T.F. He, P. Wang, Appl. Surf. Sci. 364 (2016) 249–256.
[19] J. Sundberg, H. Nyberg, E. Särhammar, T. Nyberg, S. Jacobson, U. Jansson, Surf. Coat. Technol. 258 (2014) 86–94.
[20] M. Evaristo, T. Polcar, A. Cavaleiro, Vacuum 83 (2009) 1262–1265.
[21] E. Särhammar, E. Strandberg, J. Sundberg, H. Nyberg, T. Kubart, S. Jacobson, T. Nyberg, Surf. Coat. Technol. 252 (2014) 186–190.
[22] J.R. Lince, M.R. Hilton, A.S. Bommannavar, Surf. Coat. Technol. 43–4 (1990) 640–651.
[23] K. Ellmer, C. Stock, K. Diesner, I. Sieber, J. Cryst. Growth 182 (1997) 389–393.
[24] V. Weiß, S. Seeger, K. Ellmer, R. Mientus, J. Appl. Phys. 101 (2007) 103502.
[25] D. Dumcenco, D. Ovchinnikov, O. Lopez Sanchez, P. Gillet, D.T.L. Alexander, S. Lazar, A. Radenovic, A. Kis1, 2D Mater. 2 (2015) 44005.
[26] H. Dimigen, H. Hübsch, P. Willich, K. Reichelt, Thin Solid Films 129 (1985) 79–91.
[27] G. Weise, N. Mattern, H. Hermann, A. Teresiak, I. Bächera, W. Brücknera, H.D. Bauera, H. Vinzelberga, G. Reissa, U. Kreissigb, M. Mäderb, P. Markschlägerc, Thin Solid Films 298 (1997) 98–106.
[28] F. Lévy, J. Moser, Surf. Coat. Technol. 68–69 (1994) 433–438.
[29] S. Kumar, J.T. Van Herpt, R.Y.N. Gengler, B.L. Feringa, P. Rudolf, R.C. Chiechi, J. Am. Chem. Soc. 138 (2016) 12519–12526.
[30] R. Goeke, P. Kotula, S. Prasad, T. Scharf, Sandia Report Sand 2012–5081 Unlimited Release Printed, (June 2012).
[31] M. Regula, C. Ballif, J.H. Moser, F. Lévy, Thin Solid Films 280 (1996) 67–75.
[32] H.T. Cao, J.Th.M. De Hosson, Y.T. Pei, Surf. Coat. Technol. 332 (2017) 142–152.
[33] R. Bichsel, F. Levy, Thin Solid Films 116 (1984) 367–372.
[34] F.E. Yang, Y. Lu, R. Zhang, X.H. Zhang, X.H. Zheng, Surf. Coat. Technol. 309 (2017) 187–194.
[35] T.L. Alford, Atomic Collisions and Backscattering Spectrometry, Fundamental Nanoscale Film Analysis, Springer US, Boston, MA, 2007, pp. 12–33.
[36] L. Gu, P.L. Ke, Y.S. Zou, X.W. Li, A.Y. Wang, Appl. Surf. Sci. 331 (2015) 66–71.
[37] J. Sundberg, H. Nyberg, E. Särhammar, F. Gustavsson, T. Kubart, T. Nyberg, S. Jacobsonb, U. Janssona, Surf. Coat. Technol. 232 (2013) 340–348.
[38] T. Polcar, M. Evaristo, a. Cavaleiro, Wear 266 (2009) 388–392.
[39] S. Dominguez-Meister, A. Justo, J.C.C. Sanchez-Lopez, Mater. Chem. Phys. 142 (2013) 186–194.
[40] T.W. Scharf, A. Rajendran, R. Banerjee, F. Sequeda, Thin Solid Films 517 (2009) 5666–5675.
[41] D.G. Teer, J. Hampshire, V. Fox, V. Bellido-Gonzalez, Surf. Coat. Technol. 94–95 (1997) 572–577.
[42] J. Sundberg, R. Lindblad, M. Gorgoi, H. Rensmo, U. Jansson, A. Lindblad, Appl. Surf. Sci. 305 (2014) 203–213.
[43] J.F. Moulder, J. Chastain, Handbook of X-ray Photoelectron Spectroscopy: A Reference Book of Standard Spectra for Identification and Interpretation of XPS Data, Physical Electronics Division, Perkin-Elmer Corporation, 1992.
[44] J.V. Pimentel, T. Polcar, M. Evaristo, A. Cavaleiro, Tribol. Int. 47 (2012) 188–193.
[45] R.J. Colton, J.W. Rabalais, Inorg. Chem. 15 (1976) 236–238.

[46] A. Katrib, F. Hemming, P. Wehrer, L. Hilaire, G. Maire, J. Electron Spectrosc. Relat. Phenom. 76 (1995) 195–200.
[47] L. Salvati, L.E. Makovsky, J.M. Stencel, F.R. Brown, D.M. Hercules, J. Phys. Chem. 85 (1981) 3700–3707.
[48] A. Leyland, A. Matthews, Wear 246 (2000) 1–11.
[49] Y.T. Pei, D. Galvan, J.T.M. De Hosson, J. Vac, Sci. Technol. A. 24 (2006) 1448–1453.
[50] J. Robertson, Mater. Sci. Eng. R 37 (2002) 129–281.
[51] E. Serpini, A. Rota, A. Ballestrazzi, D. Marchetto, E. Gualtieri, S. Valeri, Surf. Coat. Technol. 319 (2017) 345–352.
[52] T. Polcar, A. Cavaleiro, Thin Solid Films 519 (2011) 4037–4044.
[53] Y.X. Wu, H.X. Li, L. Ji, Y.P. Ye, J.M. Chen, H.D. Zhou, J. Phys. D. Appl. Phys. 46 (2013) 425301.
[54] J. Xu, T.F. He, L.Q. Chai, L. Qiao, X.Q. Zhang, P. Wang, W.M. Liu, Phys. Chem. Chem. Phys. 19 (2017) 8161–8173.